AIAA JOURNAL
Vol. 51, No. 1, January 2013

Vortical Interactions Behind Deployable Vortex Generator for Airfoil Static Stall Control

G. Joubert* and A. Le Pape†
ONERA — The French Aerospace Lab, 92190 Meudon, France
B. Heine‡
German Aerospace Center (DLR), 37073 Göttingen, Germany
and
S. Huberson§
CNRS — Université de Poitiers–ENSMA, 86962 Futuroscope Chasseneuil, France

DOI: 10.2514/1.J051767

An OA209 airfoil equipped with an innovative deployable vortex generator device is investigated through static stall numerical simulations. Computations are performed by solving the Reynolds Averaged Navier-Stokes equations with the elsA code, which is developed by the Office National d'Etudes et de Recherche Aérospatiale–the French Aerospace Lab. Deployable vortex generator computations are compared to a wide set of experimental data, and the actuator effect on the airfoil boundary layer is highlighted. Detailed flow analysis provides an understanding of the vortex generation mechanisms, and the influence of initial vortex interactions and merging over the control effect is shown. The influence of the deployable vortex generator thickness on static stall control efficiency is finally investigated through simulations featuring a deployable vortex generator of reduced thickness.

Nomenclature

b	=	distance between vortices, m
C_f	=	friction coefficient
C_L	=	lift coefficient
C_M	=	pitching moment coefficient
C_p	=	pressure coefficient ($\frac{\Delta p}{q}$)
c	=	airfoil chord length, m
d	=	distance from the wall, mm
e	=	deployable vortex generator thickness, mm
f, g	=	generic functions
H_i	=	boundary-layer shape factor
h	=	vortex generator reference height, mm
i	=	generic index
k	=	turbulent kinetic energy, J
M	=	Mach number
q	=	dynamic pressure ($\rho V\text{inf}^2/2$), kg.m^{-1} · s^{-2}
Re	=	Reynolds number based on the airfoil chord ($c V\text{inf}/\nu$)
$V\text{inf}$	=	freestream velocity, m · s^{-1}
Vx, Vy, Vz	=	velocity components in the x, y, and z directions, m · s^{-1}
V_n	=	vorticity normal to the surface, s^{-1}
x, y, z	=	x, y and z components
x/c	=	relative position along the airfoil
α	=	angle of attack, deg
α_S	=	static stall angle of attack of the clean airfoil, deg
δ^*	=	boundary-layer integral displacement thickness, m
Γ	=	vortex circulation, m^2 · s^{-1}
Γ^+	=	positive part of the circulation, m^2 · s^{-1}
μ_t	=	turbulent viscosity, kg.m^{-1} · s^{-1}
ν	=	kinematic viscosity, m^2 · s^{-1}
θ^*	=	boundary-layer integral momentum thickness, m

Presented as Paper 2011-1044 at the 49th AIAA Aerospace Sciences Meeting, Orlando, 3–7 January 2011; received 28 November 2011; revision received 5 September 2012; accepted for publication 11 September 2012; published online 6 December 2012.

*Ph.D. Student, Applied Aerodynamics Department; gilles.joubert@a-nse.com.
†Research Scientist, Applied Aerodynamics Department.
‡Research Scientist, Institute of Aerodynamics and Flow Technology, Helicopters Department.
§Professor, UPR 3346, PRIME Institute.

I. Introduction

DYNAMIC stall is a highly complex phenomenon occurring on helicopter main rotor blades during high-speed forward flight and maneuvers. High-blade loading and low-freestream velocities on the retreating blade side lead to massive unsteady flow separation. Depending on the airfoil characteristics and the flow parameters, dynamic stall may produce a temporary increase in drag, as well as strong negative pitching-moment peaks [1], yielding possible structural damage on the rotor. Dynamic stall is, thus, limiting helicopters' high-speed and maneuver flight capabilities. Therefore, alleviating dynamic stall has been the subject of numerous studies using different methods and control actuators [2,3]. Because the most effective control methods remain difficult to apply, none of them has been realized on real helicopter blades. Surprisingly, the vortex generator was only recently tested in this framework [4,5].

A new concept of dynamic stall control actuator (see Fig. 1) has been recently designed, built, and tested in an ONERA wind-tunnel facility, successfully reducing static and dynamic stall of an OA209 airfoil [6]. The actuator consists of a mobile row of corotating deployable vortex generators (DVGs) located at the leading edge of the airfoil (see Fig. 1). "Deployable" means that the DVG height can be controlled, getting back to clean airfoil when the height is set to zero. The DVGs are expected to induce longitudinal vortices above the airfoil in order to delay stall and to reduce the negative pitching moment while keeping a sufficient amount of lift. Although biomimetics was not leading the current device design, its outcome is expected to be similar to a humpback whale's pectoral flipper, which shows leading-edge protuberances that significantly improve the foil static stall behavior [7,8]. The DVGs also share some similarities with the Leading-Edge Vortex Generators (LEVoGs) in [4], which were likewise positioned at the airfoil leading edge and are expected to generate weak longitudinal vortices. The LEVoGs principle of operation remains, however, not fully understood and was investigated in recent studies in [9,10]. The DVG structural design implies a specific thickness of 1.0 mm, which is large compared to the

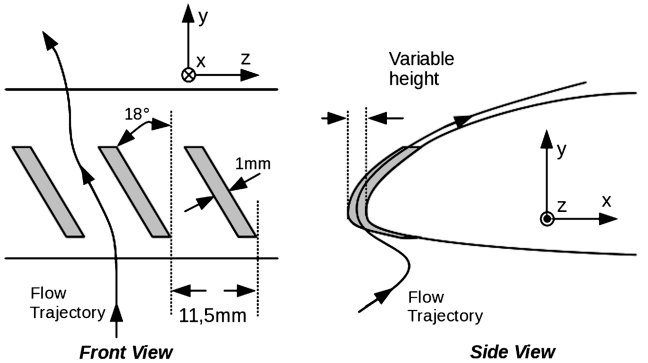

Fig. 1 Sketch of the OA209 airfoil equipped with leading-edge DVGs.

boundary-layer size, and is, therefore, expected to have some influence on the flow control. Because a detailed investigation of controlled flow could not be experimentally performed, numerical simulations are used for a deeper analysis of the flow control effect. As a first step toward future DVG dynamic stall control simulations DVG static stall control is, thereby, considered.

Since the introduction of the vortex generator (VG) as a flow control actuator in [11], such devices have been the subject of numerous studies. Schubauer and Spangenberg [12] described the mixing process capable of reenergizing the boundary layer, thus, delaying the separation created by adverse pressure gradient. Pearcey [13] reviewed the control characteristics and physics of corotating and counter-rotating vortices created from VG arrays. Much experimental and numerical work has been done to unveil the local interaction phenomenon between VG-induced vortices and the boundary layer. Viscous-inviscid interactions were considered, providing a detailed analysis of the boundary-layer turbulence characteristics in view of possible turbulence model improvement [14–16]. Lin et al. [17] and Lin [18] emphasized the benefits of VGs submerged in the boundary layer for drag reduction. This method has been quite successful in many applications and was also successfully simulated [19]. However, studies on these control actuators are either concerned with the overall flow control effect, i.e., the possible lift or drag benefit, or on the local boundary-layer and turbulence characterization aspect. The present study considers the control effect from both overall and local viewpoints altogether.

The work described in the present paper focuses on the DVG physics and the understanding of the airfoil stall control effect through numerical simulations. The objective is to identify the actual DVG flow mechanisms and its relation to the airfoil stall control. Large flow scales, as well as very fine structures, are present, which is very challenging from the numerical point of view. Steady and unsteady Reynolds Averaged Navier-Stokes (RANS and URANS) modeling through the ONERA elsA code are used. Numerical solutions are extensively validated.

The paper is organized as follows: in Sec. II, the flow parameters and the numerical methods are described; Sec. III is dedicated to the grid convergence study and the validation of the numerical simulations; and in Sec. IV, the results of DVG numerical simulations are presented, and the role of the DVG thickness is discussed.

II. Numerical Methods and Flow Parameters

A. Numerical Methods

The Computational Fluid Dynamics (CFD) solver used is the ONERA multiapplication aerodynamic code elsA [20], which solves the RANS and URANS equations for structured multiblock grids with a finite-volume method. The space discretization scheme AUSM + (P) developed in [21] is used for the inviscid fluxes. The numerical dissipation of this scheme is proportional to the local Mach number, and, thus, remains low in boundary layers. The viscous flux discretization uses a classical cell-centered formulation. For RANS calculations, the pseudotime backward Euler scheme is selected. For URANS computations, a second-order implicit time discretization method with Low-Up (LU) factorization and Newton iterations is applied. In the present work, the two-equation k-ω model with Kok cross-derivative terms is used. The Shear Stress Transport (SST) correction in [22] and the turbulent dissipation rate limiter of Zheng are also used. In case of clean (i.e., without DVG) computations, the Arnal–Habiballah–Delcourt transition criterion in [23] is used. It provides a model for laminar separation bubble transition and has been successfully used in similar work in [24]. For DVG computations, laminar-turbulent transition is presumed to be triggered by the VG at its most upstream position. Thus, the flow is supposed fully turbulent, and the laminar-turbulent transition is not not accounted for. External boundary conditions are of the nonreflecting type and are applied 20 chords away from the airfoil.

B. Geometry and Flow Conditions

Numerical investigations are performed on the rotor blade airfoil OA209 [25] equipped with a row of corotating DVGs. The DVG is a 1.0-mm-thick blade extruded from the leading-edge surface in the chordwise direction. The angle with the vertical reference is 18. The DVGs are spaced equidistantly at 11.5 mm in the spanwise direction (Fig. 1). For a DVG height of $h = 0$ mm the airfoil is similar to the clean case and has no control effect. Experimental results in [6] on the same configuration showed a large influence of the DVG height on static stall control, and 1.5 mm has been found to be the best value for pitching moment reduction. The DVG height is, therefore, fixed to 1.5 mm in the present study.

Reynolds and Mach numbers are set to $Re = 1.8 \times 10^6$ and $M = 0.1617$, respectively. These parameters are taken from previous static and dynamic stall studies [26].

C. Specific Postprocessing

To analyze the generated vortices and their characteristics a specific tool has been developed and can extract vorticity in slices normal to the airfoil surface (Fig. 2). The main vortex produced by the

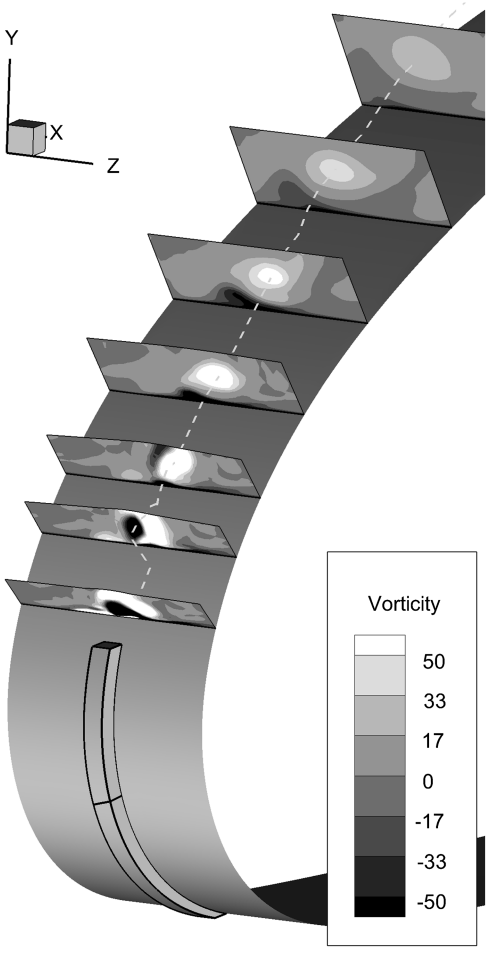

Fig. 2 Vorticity slices and vortex trajectory along the airfoil.

DVG rotates in the clockwise direction. Therefore, the positive circulation is integrated for each slice allowing quantitative comparisons between different VG computations. For a contour ∂S closing the surface S traversed by the velocity $\mathbf{V}$, the circulation Γ is defined as follows and expressed as a function of the curl of the velocity:

$$\Gamma = \oint_{\partial S} \mathbf{V}\,\mathrm{d}s = \int_S \mathbf{rot}(\mathbf{V}) \cdot \mathbf{dS} \tag{1}$$

where **dS** is the local vector normal to the surface S. Hence, only the vorticity component normal to the plane V_n is accounted for. Vorticity is transported streamwise above the airfoil, and the corresponding vorticity axis is assumed to be close to each slice's normal direction. The positive part of V_n^i integrated over the discrete element of surface ΔS is then expressed as

$$\begin{cases} \Gamma^+ = \displaystyle\sum_i V_n^i \Delta S_i \\ \text{if } V_n^i < 0 \quad \text{then } V_n^i = 0 \end{cases} \tag{2}$$

The positive circulation can be used to analyze the vortex strength and its streamwise dissipation rate.

III. Clean Reference, Mesh Convergence, and Validation

A. Clean Reference Case and Convergence Discussion

The large influence of the mesh on numerical simulations of airfoil at stall or near-stall conditions is well known. For NACA0015 static and dynamic stall numerical simulations, the influence of two-dimensional (2-D) mesh refinement was investigated [27,28] from which a grid with 1900 nodes around the airfoil was selected. However, considering future three-dimensional DVG meshes numerical simulations using such fine grids would not be affordable. Considering the present exploration-oriented work, a coarser grid is necessary. Thus, this section is dedicated to the evaluation of a less refined 2-D mesh, which will be used 1) to provide a computational reference case for a clean airfoil (i.e., without DVG) and 2) as the basis for the DVG mesh development.

Clean case computations are performed on a 2-D grid of an OA209 airfoil. The main block size is 501×121 nodes with 316 nodes around the airfoil (Fig. 3). This mesh includes the airfoil tab in which the thickness is discretized with 33 nodes, and the tab surface is modeled with a sliding-wall boundary condition. From the mentioned studies this simplification is not presumed to alter significantly the solution and provides an appreciable savings on grid size. Using the above described numerical methods and parameters computations of the flow around the 0A209 airfoil at static angles of attack (AoA) are performed.

The convergence evaluation of the solution is not an easy task and has to be discussed in order to consider the computations' validity. The first criterion used are the residuals of the conservative variables, which are expected to tend toward zero, at least decreasing of three orders of magnitude. However, due to the presence of the airfoil trailing-edge tab, a small recirculation is observed downstream of the tab. For $\alpha = 10$ deg this recirculation remains steady, and the residual convergence level of the computation is very satisfactory. For $\alpha = 12$ deg, 15 and 16.7 deg the tab recirculation begins to slightly oscillate from iteration to iteration. The flow is physically unsteady, and the residuals cannot decrease but reach a saturation level. However, the lift coefficient variation tends to stabilize around a mean value (Fig. 4a). The ratio $\Delta C_L / C_L$ remains very low for the considered AoA, showing that a mean steady flow is predominant (Fig. 4b). The convergence criterion is not satisfied, but the steady solution can be considered as a satisfactory approximation and remains in excellent agreement with experimental pressure data for $\alpha \leq 16.7$ deg (Fig. 5). From $\alpha = 17.2$ deg, however, the lift variations are much larger, and the flow unsteadiness must be taken into account.

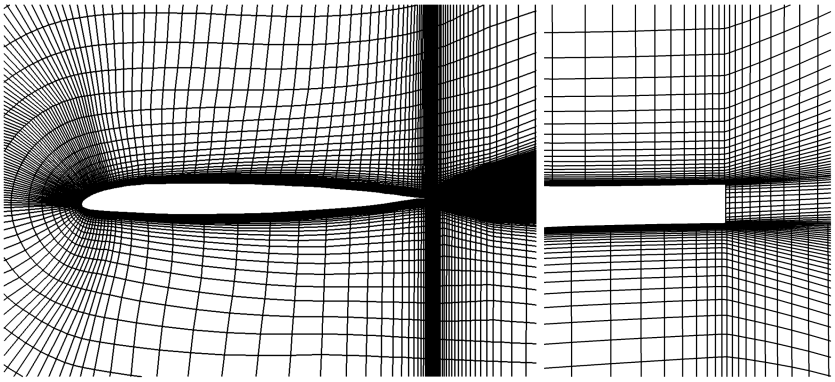

Fig. 3 0A209 clean airfoil 2-D mesh with tab detail; every other second point is displayed.

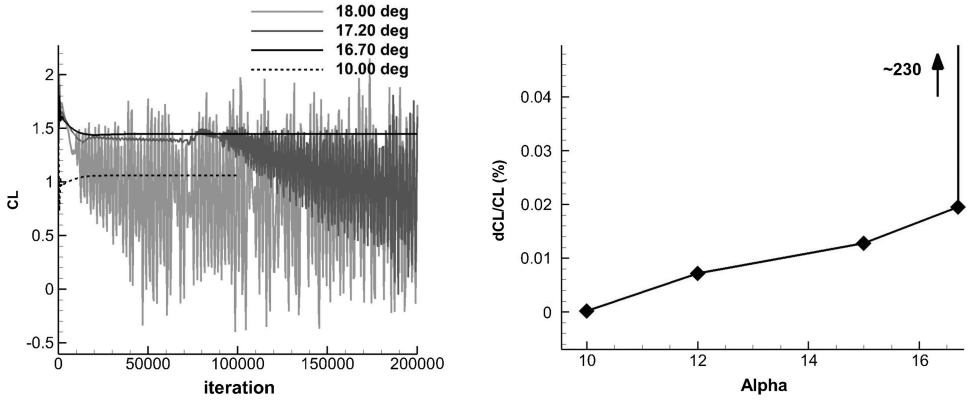

a) Clean RANS lift variations **b) Clean RANS computation convergence ratio**

Fig. 4 Clean RANS computation convergence.

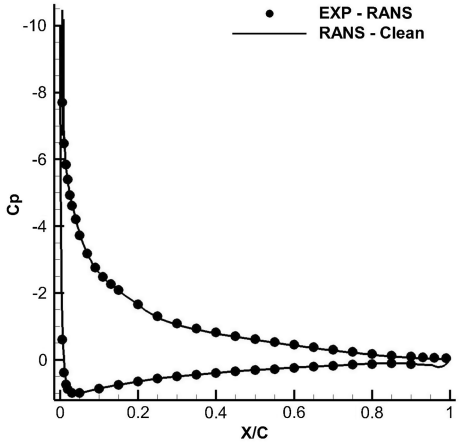

Fig. 5 Clean RANS pressure compared with experimental data at $\alpha = 16.7$ deg.

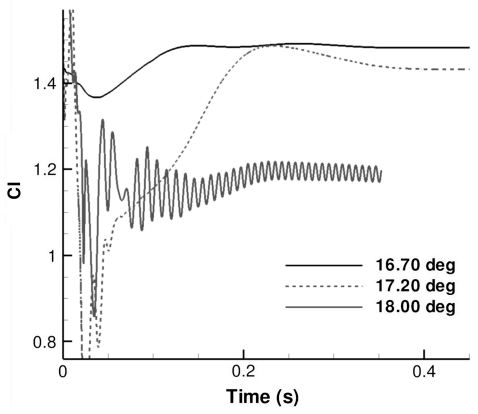

Fig. 6 Clean URANS lift temporal evolution.

Further numerical simulations are performed using the URANS method for $\alpha = 16.7$ deg, 17.2 deg, and 18.0 deg with a time step $\Delta t/c \times V\,\text{inf} \sim 10^{-4}$, providing at least one order of magnitude of residual decrease in the Newton subiterations. For $\alpha = 16.7$ deg the mean value of the unsteady lift coefficient is very close to the steady lift coefficient with a difference lower than 0.5% (Fig. 6). For $\alpha = 17.2$ deg the simulation also reaches a steady solution. For $\alpha = 18$ deg the time variations of the lift indicate an unsteady flow. Those large improvements achieved by URANS computations can be explained by some specificity of the steady RANS resolution. To provide convergence acceleration the steady RANS method uses a local time step dependent on the cell size. Thus, the solution convergence rate can be different from cell to cell; artificial gradients may occur and hamper the residual convergence, which leads to nonphysical solutions. Using a global time step the URANS method avoids this problem, and the problem remains well posed.

For the present mesh and flow parameters the solution is mathematically converged if $\alpha \leq 10$ deg. For $12 \leq \alpha \leq 16.7$ deg the steady solution is not converged but can be taken as a fair approximation of the unsteady-calculated solution. This greatly reduces the computational cost, because the computational cost of unsteady calculations is about 100 times higher than for steady calculations. From $\alpha \geq 17.2$ deg unsteady computations are necessary. This methodology can be summarized in Fig. 7 as a combination of steady and unsteady solutions.

The lift and pitching moments are compared to experimental data (Fig. 7). For $\alpha \leq 15$ deg the steady numerical simulation is in very good agreement with the experimental measurement. For $\alpha \geq 16.7$ deg the computed clean airfoil does not present the sudden loss of lift and drastic decrease of the pitching moment. The computations are not able to reproduce the airfoil leading-edge stall. This is not unexpected, because two-equations turbulence models are known to produce an excessive amount of turbulent viscosity μ_t, thus, delaying separation and altering the flow topology. Using the Menter SST correction and the Zheng limiter the excess of μ_t is slightly reduced. Nevertheless, the present static stall simulation remains inaccurate for $\alpha > 15$ deg. In the framework of the DVG control capability evaluation, these 2-D computations will be taken as a clean reference case for AoA lower than static stall, $\alpha_S \sim 15$ deg, only.

B. Deployable Vortex Generator Case and Convergence Discussion

The grids used for the DVG computations are all based on the previously described 2-D grid. The block topology is aligned with the DVG direction (Fig. 8), which provides a limited mesh distortion and adapted cell size on each side of the DVG. Only one DVG is included

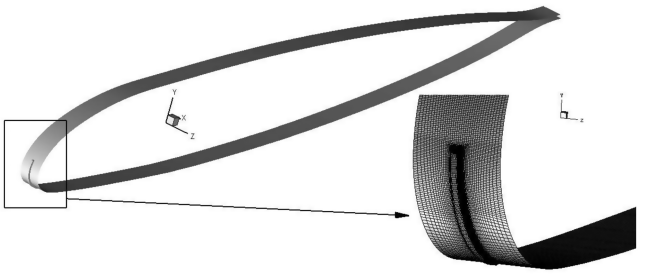

Fig. 8 View of the DVG and airfoil mesh surface.

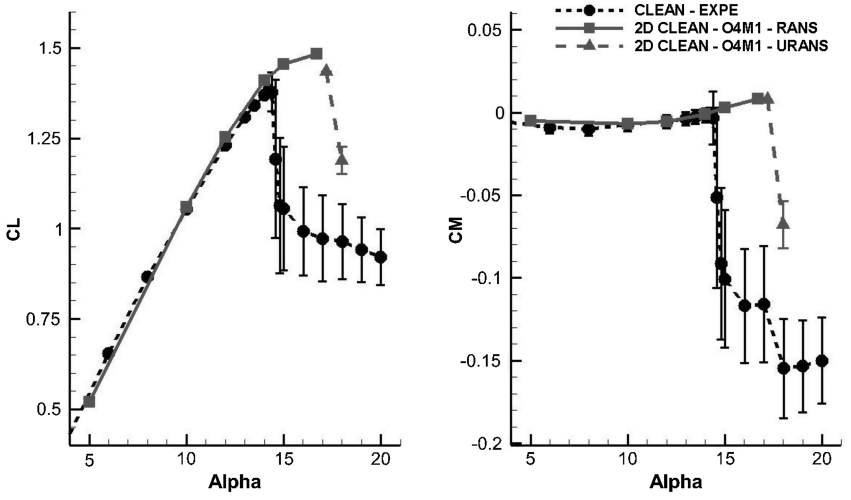

Fig. 7 Lift and moment coefficient polars for clean steady and unsteady computations.

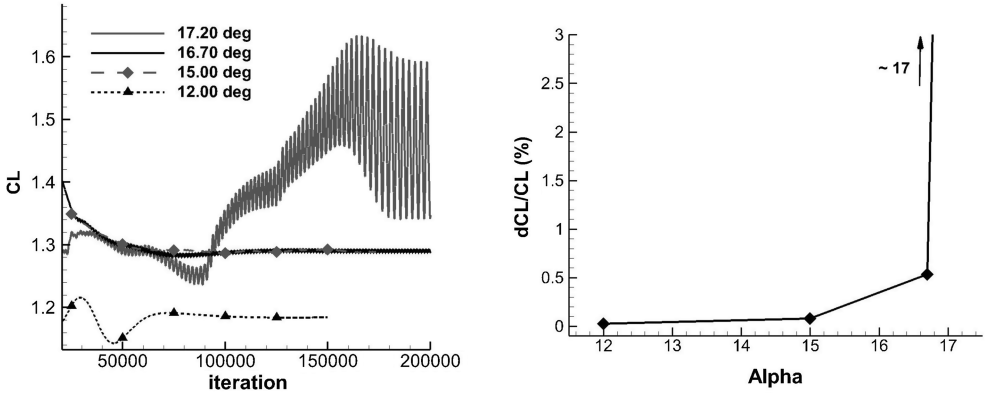

a) DVG RANS computations lift variations b) DVG RANS computations lift ratio

Fig. 9 DVG RANS computations convergence.

in the grid with a spanwise length that represents 2.3% of the chord. A periodic boundary condition is used between the lateral mesh borders in order to take the DVG spatial periodicity into account and allow possible transverse flows.

Preliminary DVG computations are performed, which meet the same convergence issue. Concerning clean case simulations the tab initiates unsteadiness and prevents residual convergence. Adding the DVG geometry in the simulation results in additional flow unsteadiness. However, because the DVG thickness is of the same order of length, the unsteady behavior is expected to have the same effect as the reported tab unsteadiness. The lift coefficient convergence of the DVG steady simulations proves to be satisfactory for $\alpha \leq 16.7$ deg (Fig. 9a). The $\Delta C_L/C_L$ ratio is compared for steady computations (Fig. 9b) and provides a criterion in order to set the choice of steady or unsteady simulations.

For further DVG computations the following methodology is selected: for $\alpha \leq 15$ deg the RANS convergence is satisfactory; for $\alpha \geq 17.2$ deg the URANS modeling is necessary. Regarding the computations at 16.7 deg steady and unsteady preliminary computations topologies are strongly similar, and the pressure distribution and aerodynamic coefficient comparison presents only small discrepancies (~3% at the suction peak). Thus, in order to reduce the computational cost, steady RANS simulations are performed at 16.7 deg in the next grid sensitivity study section. However, because it provides slightly more accurate results, URANS computations shall be used for further detailed flow analysis.

C. Deployable Vortex Generator Grid Sensitivity Study

The chordwise mesh refinement is not considered in the current study. The influence of two grid parameters are investigated in this section: 1) the boundary-layer refinement over the DVG walls and 2) the overall discretization in the airfoil spanwise direction. The AoA of 16.7 deg is close to but lower than α_S, and it is selected for the grid refinement investigations for which steady computations are performed.

To evaluate the refinement in the boundary layer of the DVG walls simulations performed on three different meshes are compared (Table 1). The size of the first cell to the wall can be tested thanks to the $y+$ values. For each tested grid the airfoil wall discretization was proved sufficient, which is shown by the maximum $y+$ values below 2.5 over the airfoil surface and for the attached flow. Then, as reported in Table 1, the initial mesh simulation presents high $y+$ values (up to 7) over the DVG walls, which is usually too high to get an accurate boundary-layer solution. Using finer meshes the simulations show $y+$ values below 3, which is usually considered as satisfactory. However, neither the vortex circulation analysis (Fig. 10a) nor the pressure coefficient (Fig. 10b) present noteworthy discrepancies between the three tested meshes. With mesh refinement the simulation is expected to better take into account the generated vortex influence over pressure. Nevertheless, the vortex strength and position are not modified with the grid refinement, thus, the reported pressure distributions are strongly similar for all meshes. Hence, the DVG wall refinement does not have a significant effect on the results, and the coarser grid will be used for further computations.

Table 1 Meshes discretization and $y+$ values in the boundary-layer zone of the DVG

Mesh name	Initial mesh	Mod 2	Mod 3
Number of points in the DVG surrounding O block	19	26	33
Number of points in spanwise direction	37	37	61
$y+$ maximum value observed on the airfoil leading-edge wall ($\alpha = 16.7$ deg)	2.4	2.1	2.1
$y+$ maximum value observed on the DVG walls ($\alpha = 16.7$ deg)	6.9	2.8	1.9

The influence of grid refinement in the spanwise direction is then considered with five grids with different spanwise discretization (Table 2). The airfoil lift coefficient differs by ~12% between the coarsest and the finest grid (Fig. 11), which illustrates the influence of this refinement on the solution. With increasingly finer grids the lift decreases with a monotonic and asymptotic behavior. For the considered parameters a mesh with at least 61 points in the spanwise direction should be used in order to alleviate the grid influence on numerical solutions but would lead to a very high-computational cost. A cost-to-precision compromise is found with a 37-spanwise points grid for a small relative error (2%) on the lift coefficient. Further calculations are then performed using this best compromise, i.e., the initial mesh.

D. Extensive Validation Through Comparison with Experimental Data

The DVG computations are compared to experimental data through three experimental sets of data: 1) pressure measurements along the airfoil chord and aerodynamic coefficients, 2) laser Doppler velocimetry (LDV) in a small window placed above the leading edge of the airfoil, and 3) time-averaged particle image velocimetry (PIV) of the flow above the whole airfoil suction side.

1. Surface Pressure Comparison

Pressure distributions of the 2-D clean reference and DVG fully turbulent solutions are compared along with experimental pressure data (Fig. 12) at $\alpha = 15.0$ deg. Both clean and DVG computations are in fair agreement with each experimental data set; the overall effect due to the VG presence is then satisfactorily reproduced.

Table 2 Spanwise discretization of the meshes used for the DVG grid refinement study

Mesh name	Coarsed 2	Coarsed 1	Initial mesh	Mod 3	Mod 4
Number of points in spanwise direction	21	29	37	61	79

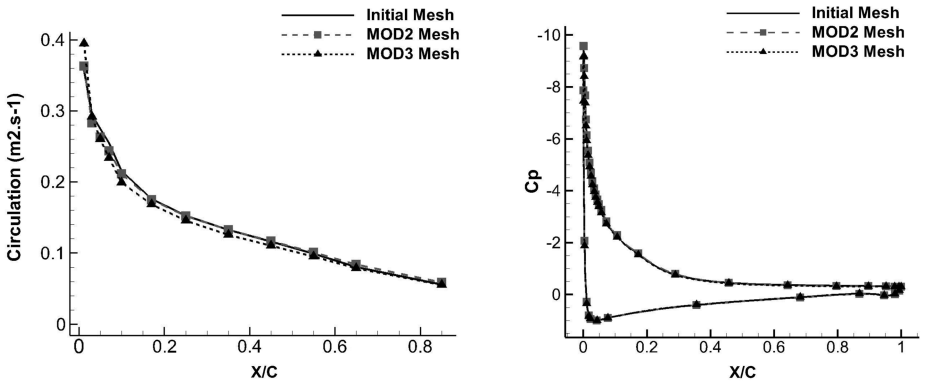

a) Circulation decay comparison b) Pressure coefficient comparison

Fig. 10 DVG mesh refinement comparison for $\alpha = 16.7$ deg.

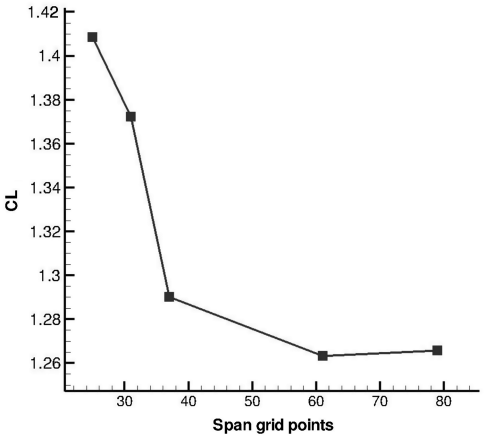

Fig. 11 C_L comparison for different spanwise mesh refinements at $\alpha = 16.7$ deg.

Furthermore, this strengthens the fully turbulent hypothesis selected for the DVG computations.

The experimental lift and moment coefficients are estimated through pressure integration [6] and are compared to computational lift and pitching moment coefficients (Fig. 13). Following the previous convergence analysis conclusions the AoA of 16.7 deg, 17.2 deg, and 18 deg are computed using the URANS method. The error bars are, respectively, the standard deviation for experimental data and min-max values for numerical results. Between 12 deg and 16.7 deg, the simulation is in good agreement with the experimental lift and pitching moment coefficients. The min-max values are small, and the temporal variations of the numerical solution remain limited. At 17.2 deg, lift stall is observed in the simulation, which means an underestimation of the stall AoA experimentally observed at 17.8 deg. However, the lift loss at stall for both simulations, (∼6%) and experiment (∼7%), are of the same order of magnitude. At 18 deg the numerical lift coefficient is overestimated, and the negative pitching moment coefficient is largely underestimated. More importantly, the large computational min-max value emphasizes the strong unsteadiness of the flow.

Up to the $\alpha = 18$ deg, the numerical simulation is in fair agreement with the experiment and proves particularly capable to give the correct pitching moment showing a slight increase at 15 deg and a progressive decrease from 15 deg to 17.2 deg. At 18 deg, however, the simulation is far from the experimental result. Nevertheless, the DVG computations are in much better agreement with the experimental data than the clean case simulations for the considered AoA.

2. *Laser Doppler Velocimetry Velocity Field Comparison*

The LDV gives access to averaged velocity in a window above the leading-edge region of the airfoil at the spanwise position of the DVG downstream edge (Fig. 14). Data extraction at $x/c = 0.08$ provides an accurate comparison of experimental and numerical velocities and is presented in Fig. 15. The normalized experimental turbulent kinetic energy $k/V\,\mathrm{inf}^2$ is computed from the standard deviation (root mean square or rms) values of the velocity components.

The Vx/V inf computational velocity outer field is in very good agreement with the LDV data (Fig. 15a). Moreover, the abrupt increase of $k/V\,\mathrm{inf}^2$ close to the wall in Fig. 15b gives access to the boundary-layer outer limit, and the agreement between numerical and experimental data is excellent. However, the LDV field discretization is not fine enough in the DVG-induced vortex zone to

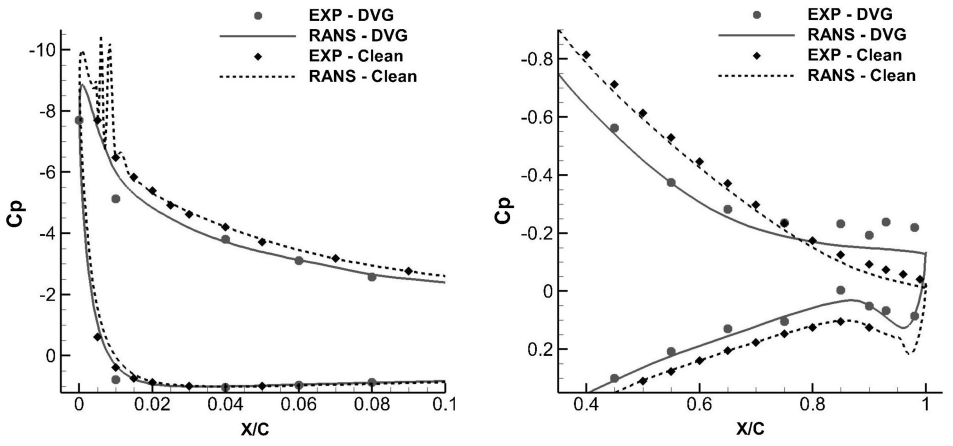

a) Leading-edge detail b) Trialing-edge detail

Fig. 12 Pressure comparison between calculations (lines) and experimental data (symbols) for baseline and controlled cases at $\alpha = 15$ deg.

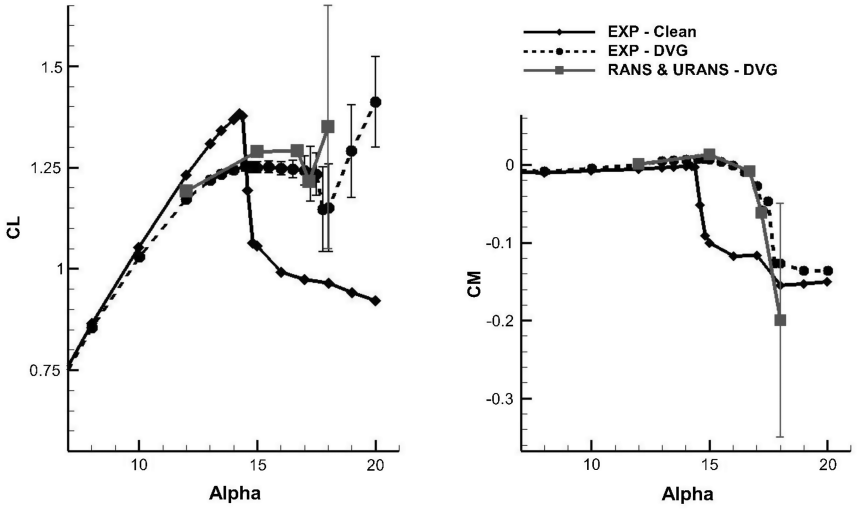

Fig. 13 Experimental and computational polars.

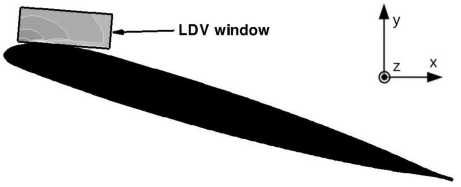

Fig. 14 LDV window over the airfoil.

allow quantitative comparisons; the transverse velocities Vz/V inf of the numerical solution in Fig. 15c shows negative then positive peaks corresponding to the vortex. In the LDV data the velocity gradient is discretized over two measurement positions only.

Experimental estimation of $k/V\,\mathrm{inf}^2$ must be considered with caution, because this so-called turbulent kinetic energy is computed using rms values whose correlation with turbulent fluctuations is not clear. Moreover, the rms values are dependent on the time scale of the captured variations. In LDV measurements the acquisition time length (normalized by the chord advection time $c/V\,\mathrm{inf}$) $\Delta t \times V\,\mathrm{inf}/c$ lies between 110 and 2200 depending on the acquisition position. rms values can then include velocity variations due to the possible presence of coherent structures in which connection to the turbulence remains uncertain. Thus, the present experimental $k/V\,\mathrm{inf}^2$ variable more likely represents the *temporal velocity variations* than turbulence kinetic energy. Furthermore, the compared URANS solution is not time averaged and possible additional temporal variations are not taken into account by the numerical turbulent kinetic energy. Nevertheless, the simulation turbulence model production of $k/V\,\mathrm{inf}^2$ is physically correlated with the temporal velocity variations, and qualitative comparison with experimental data is possible.

3. *Particle Image Velocimetry Velocity Field Comparison*

The main drawback of the previously presented LDV results is the small size of the window available for flow velocities comparisons. To better assess the computation validity averaged PIV covering the whole upper side of the airfoil flow are used. For accurate comparison slices of the numerical solution are generated, where the position matches the PIV laser sheet. The right-top corner of every PIV field, however, is erroneous, because the laser sheet did not illuminate this part of the flow. For further information about the experimental apparatus the reader is referred to [9] describing the PIV setup used. The current PIV field is averaged over time and provides 2-D–2-C velocity measurements. The averaging process gives also access to the velocity rms values. The numerical simulations are compared with PIV for two AoA: 15 deg (Fig. 16) and 17.2 deg (Fig. 17). The PIV results for 12 deg and 16.7 deg are not shown but mentioned in the discussion.

At 12 deg and 15 deg the numerical simulation is in good agreement with the PIV. The experimental and numerical Vx/V inf contours match fairly well in Fig. 16a, and the trailing-edge separation occurring in the PIV field is also accurately reproduced by the numerical simulation. Some discrepancies are observed for turbulent kinetic energy $k/V\,\mathrm{inf}^2$ between the simulation and PIV measurements (Fig. 16b). Nonetheless, the experimental $k/V\mathrm{inf}^2$ was estimated using rms values of the velocity components and is, therefore, strongly affected by the time resolution of the PIV. In the present case, frequencies higher than 1050 Hz could not be measured. Moreover, as discussed previously in the LDV measurement analysis, one must use caution for the quantitative comparison of the turbulence model kinetic energy with respect to the experimentally estimated $k/V\,\mathrm{inf}^2$. Hence, the location of the regions of large PIV *temporal velocity variations* and the high-computational $k/V\,\mathrm{inf}^2$ values are in

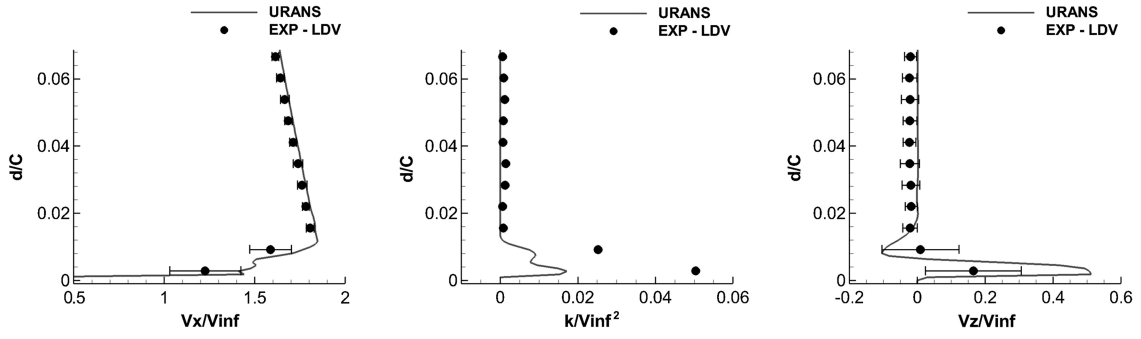

a) Vx/Vinf **b) k/Vinf^2** **c) Vz/Vinf**

Fig. 15 Comparison of LDV data and numerical results; the distance *d* from the wall is normalized by the chord length, and experimental error bars correspond to rms values.

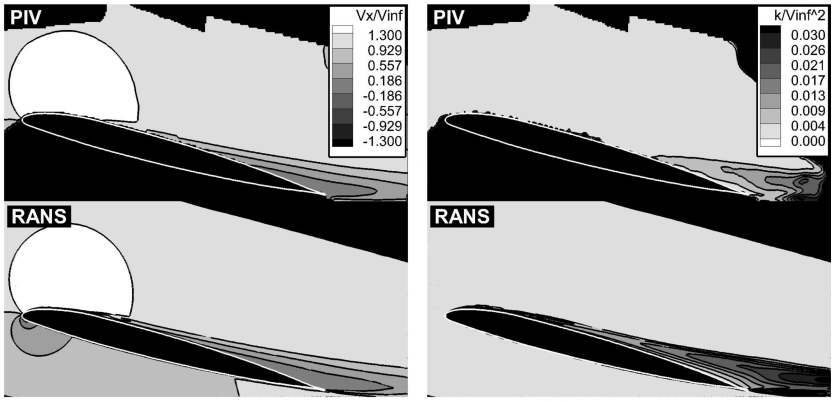

a) $Vx/V\text{in}f$ b) $k/V\text{in}f^2$

Fig. 16 Experimental PIV (top) and RANS computation (bottom) for $\alpha = 15$ deg.

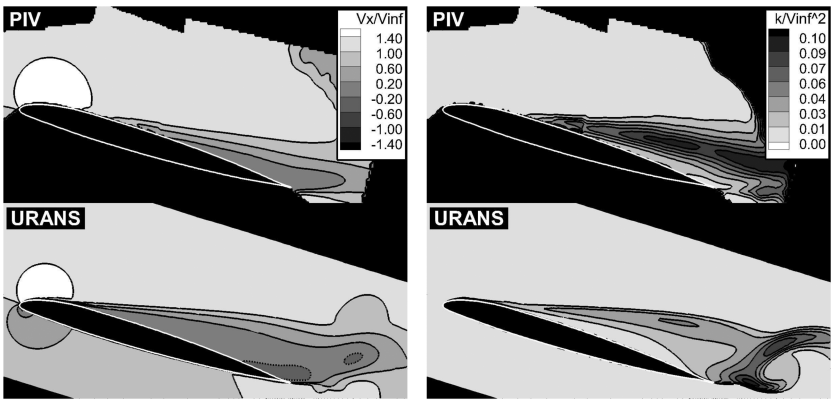

a) $Vx/V\text{in}f$ b) $k/V\text{in}f^2$

Fig. 17 Experimental PIV (top) and RANS computation (bottom) for $\alpha = 172$ deg.

excellent agreement, showing that the turbulence model is qualitatively accurate for the considered AoA.

At 16.7 deg to a smaller extent and at 17.2 deg to a larger extent the numerical solution differs from the PIV measurement. Vortex shedding can be observed downstream of the trailing edge within the numerical flow in Fig. 17a. It must be noted that URANS numerical solutions are not time averaged, which may increase the discrepancies between numerical solutions and experimental data. The recirculation region is clearly overestimated, and the separation point is located further upstream in the simulation than in the PIV measurement. Considering the clean case a leading-edge separation is expected at α_S, producing the typical stall sudden lift decrease. In the controlled configuration the flow remains partially attached for $\alpha > \alpha_S$ and shows a smoother stall associated with trailing-edge separation. Because of the DVG presence the airfoil stall behavior is changed from leading-edge to trailing-edge type.

The differences between simulations and experiments are summarized by the separation location variation as a function of the AoA (Fig. 18). The simulation overestimates the separated region size, which leads to earlier stall compared to the experiment but the overall trailing-edge stall behavior is fairly well reproduced.

IV. Results and Discussion

A. Overall Control Effect Analysis

To analyze the overall effect of the DVG on the airfoil boundary layer numerical flow solutions of the 2-D clean case and the DVG case are compared for $\alpha < \alpha_S$ of the clean case at $\alpha = 15$ deg. The DVG flow is fully 3-D, and for appropriate comparison the DVG solution is averaged in the spanwise direction, thus, providing a 2-D flow solution. The span-averaged velocity and turbulent kinetic energy profiles of the clean and DVG cases are compared (Fig. 19). At $x/c = 0.85$ the clean case remains attached, and the DVG case shows a recirculation (Fig. 19c). The boundary-layer thickness δ can be defined for $Vx = 0.99 \times V$ max with V max as the highest local x velocity. Because of the vortex presence near to the wall a velocity deficit and vorticity increase are observed. The boundary-layer thickness is then clearly larger in the DVG case, which has to be taken into account for the evaluation of the capability of the boundary layer to resist an adverse pressure gradient.

Downstream of the DVG the boundary-layer integral thicknesses provide essential information about the DVG-induced vortex influence and the near-wall flow. The integral thickness values are the displacement thickness δ^*, the momentum thickness θ^*, and the shape factor H_i. These quantities are defined as follows:

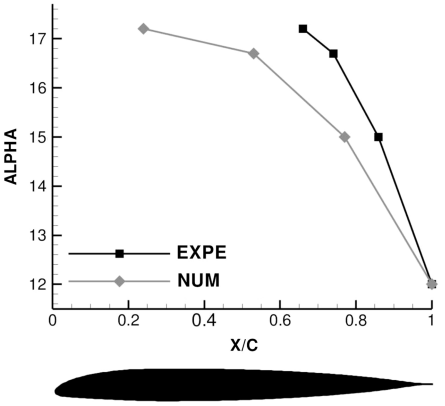

Fig. 18 Separation point chordwise location.

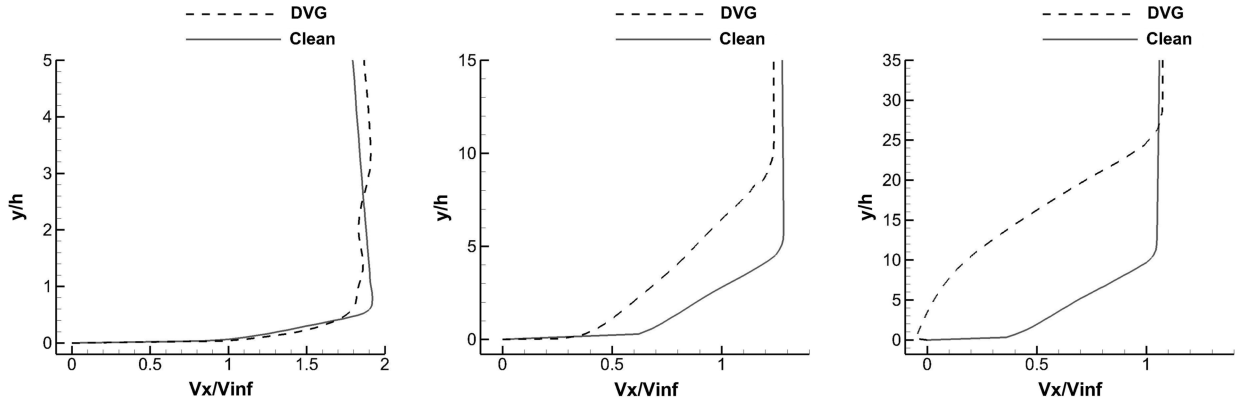

Fig. 19 Velocity $Vx/V\,\mathrm{inf}$ at three chordwise locations $\alpha = 15$ deg.

$$\delta^* = \int_\delta \left(1 - \frac{V(y)}{V\,\mathrm{inf}}\right) \mathrm{d}y;$$

$$\theta^* = \int_\delta \left(1 - \frac{V(y)}{V\,\mathrm{inf}}\right)\left(\frac{V(y)}{V\,\mathrm{inf}}\right) \mathrm{d}y; \qquad H_i = \frac{\delta^*}{\theta^*} \tag{3}$$

The displacement thickness δ^* can be interpreted as the inverse measure of the boundary layer's inertia. With small δ^* the boundary layer has a high inertia and a small sensitivity to the adverse pressure gradient. The momentum thickness θ^* is a measure of the boundary-layer energy. If θ^* is high, the boundary-layer sensitivity to the adverse pressure gradient is low. The shape factor H_i summarizes the boundary-layer capability to resist to the adverse pressure gradient. If H_i maintains low values the boundary layer remains attached longer. If it reaches values higher than 4 this is an indication of boundary-layer separation.

The overall DVG influence on the airfoil upper side separation is summarized thanks to the longitudinal shape factor H_i variations (Fig. 20). The clean case shows a higher shape factor than the DVG case from the leading edge up to 45% of the chord. This clearly demonstrates the DVG positive influence, because lower shape factor values are related to the boundary layer's higher resistance to the adverse pressure gradient. Downstream at 50% chord the DVG case's boundary layer is more sensitive to the adverse pressure gradient and separates earlier compared to the clean case. An explanation for this sensitivity is proposed in the next section.

The overall effect of the DVG on the airfoil stall may also be considered as stall-behavior modification. The OA209 clean airfoil stalls for the given conditions from the leading edge, with a sudden loss of lift at a critical AoA, where the airfoil suction side is almost fully separated. This situation is modified by the DVG addition as the controlled airfoil stalls from the trailing edge. It has been observed that the boundary-layer characteristics are strongly modified by the presence of the DVG-induced vortex. Because subsonic flow lets information and the history of the boundary layer at the trailing edge be transported upstream the whole airfoil circulation is, thus, affected by the DVG presence. Change in the stall behavior is then likely a consequence of the airfoil boundary-layer modification.

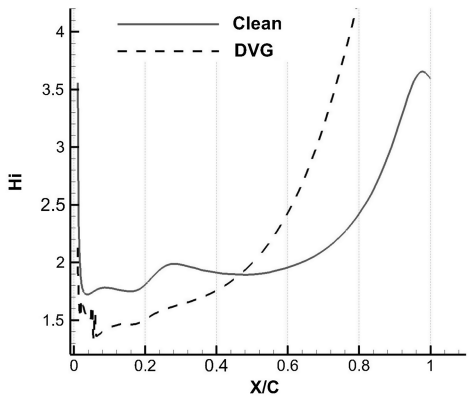

Fig. 20 Shape factors H_i of clean and DVG cases along the airfoil chord $\alpha = 15$ deg.

B. Vortex Generation Analysis

To better understand the physics involved in the DVG effect a detailed flow analysis around the DVG is performed. Interestingly, the flow topology appears to be more complex than expected for a regular VG geometry (Fig. 21). A complex vortical system can be observed and described as follows:

1) Two positive corotating vortices P1 and P2 are generated from both longitudinal edges of the DVG, and they merge approximately a half DVG length downstream, forming the *main positive vortex.*

2) A negative vortex N1 occurs between P1 and the DVG.

3) At the downstream edge of the DVG a small positive vortex P3 is visible.

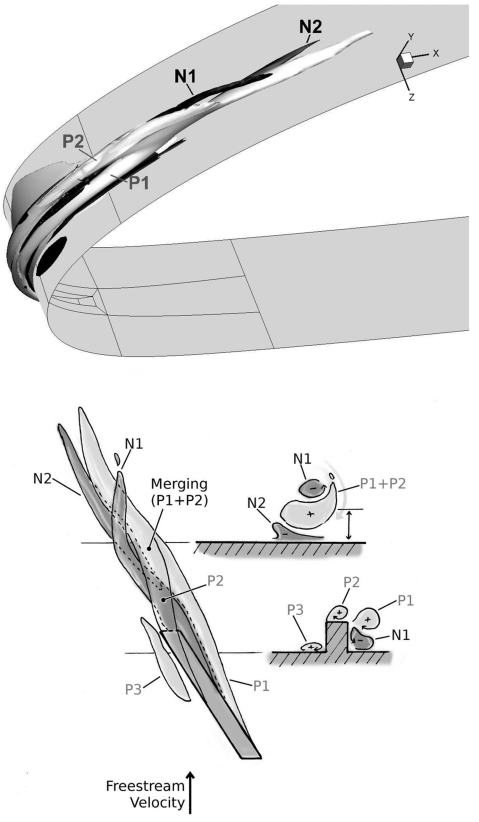

Fig. 21 DVG flow: (top) isosurfaces of helicity and (bottom) topology sketch. Helicity is defined as the scalar product of vorticity and velocity.

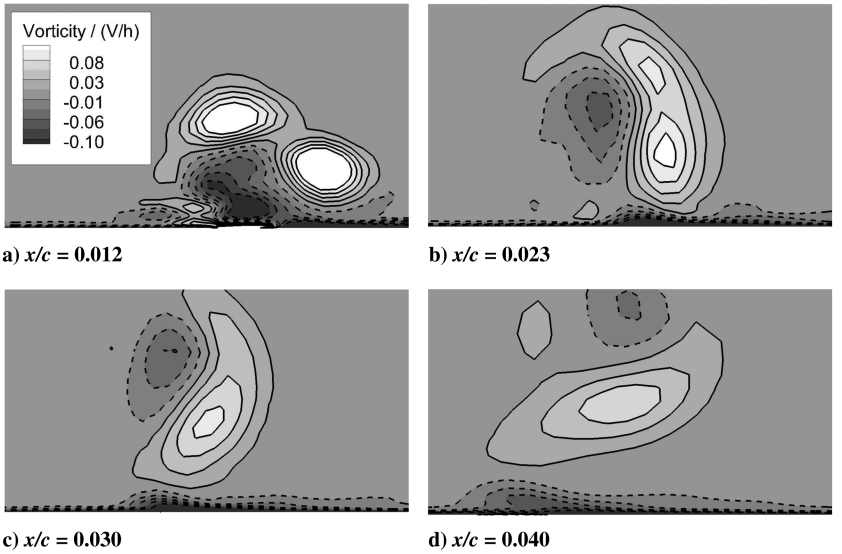

a) x/c = 0.012 **b) x/c = 0.023**

c) x/c = 0.030 **d) x/c = 0.040**

Fig. 22 Vorticity normal to the slice at various x/c or vortex ages $\alpha = 16.7$ deg.

4) A second negative vortex N2 occurs downstream of the DVG between the main positive vortex and the airfoil wall.

The whole vortical system is convected downstream by the main flow. An orbital motion is induced by the merging vortices, and N1 revolves around them as illustrated by the scheme in Fig. 21 and by the flow slices in Fig. 22.

To the authors' knowledge such a complex system of vortices has never been reported in the framework of VG numerical or experimental studies. However, the actual flow is very similar to the wing-tip vortex of a flat end-cap wing. In an experimental study in [29] and more recent computational work in [30] the flow topology analysis shows two main positive vortices, respectively, detaching from the upper and lower edges of the wing cap. A stronger, primary vortex occurs on the upper wall of the wing, and a secondary vortex occurs from the lower side of the cap. The vortices merge shortly downstream of the wing, leaving only one wake vortex. Such a description fits very well with the present DVG flow observation, however, no reference to significant negative vortices was mentioned. These negative vortices are to be connected to the presence of airfoil walls. In a review dedicated to wall-vortex interaction phenomena the side effects were emphasized of the vortex influence on the boundary layer [31], which usually generates vorticity of the opposite sign to that of the main vortex. Thus, P1 and its resulting main positive vortex, respectively, induce the negative vortices N1 and N2 as counterparts from local surfaces interactions.

Downstream of the DVG the relative revolution of vortical structures around each other and their merging constitute a distinctive aspect of the interaction of the corotating vortices. Meunier et al. [32] states three successive phases that characterize the merging process of corotating vortices: 1) a first stage where both vortices orbit at quasi-constant distance from a common barycenter, 2) a second stage where the separation distance collapses, and 3) a third stage where significant nonaxisymmetric perturbations still exist at the center of the newly formed vortex. This description is related to corotating vortices that are initially identical in circulation and size and without any wall influence, which is not the case in the present flow. Nevertheless, the variation of the intervortex distance in Fig. 23a fits qualitatively very well with the previous merging description. The rotating motion induced by the corotating interaction combines with the previously mentioned wall-vortex interaction. Thus, a large amount of negative vorticity is swept away from the boundary layer toward the outer region of the flow. This is the reason for the main negative vortex to move around the corotating system, which also induces local boundary-layer separation. Finally, the overall effect of the corotating interaction can be underlined by Fig. 23b where positive circulation decay rate is spatially correlated with the merging process, because the decay rate change occurs as the merging is over.

The circulation decay is related to wall friction slowing the vortex rotation. From this, chordwise variations of the circulation decay rate are analyzed and described as three successive stages in Fig. 24. In the *corotating stage* (C stage), the corotating vortices' interaction increases the overall rotating motion and the wall friction, and the circulation decay rate is at its highest level. This stage ends with the vortex merging at $x/c \approx 0.03$. In the second *negative stage* (N stage) the main positive vortex remains confined close to the wall by the negative vortex N1 until $x/c \approx 0.1$, and the circulation decay rate is moderate. When the negative vortex revolution is complete, the third *viscous stage* (V stage) begins; the main positive vortex is only subject to physical and turbulent viscosity, and the circulation decay rate is the lowest.

This circulation history provides an explanation for the separation occurring at the airfoil trailing edge for prestall AoA. Because of the rotational motion the main positive vortex transfers high momentum from the external flow to the boundary layer, and the boundary layer is less sensitive to the adverse pressure gradient in comparison to the

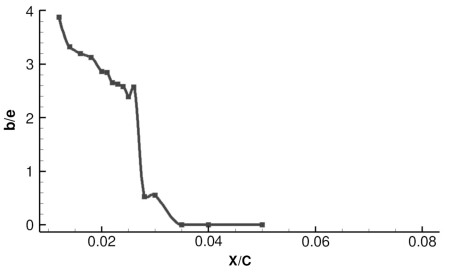

a) Distance *b/e* between positive vortices

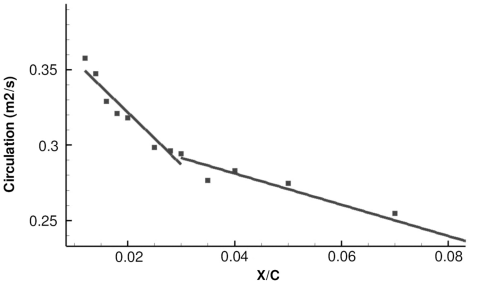

b) Positive circulation

Fig. 23 Vortex merging process along x/c. The airfoil leading edge is at $x/c = 0$, and the DVG most upstream position corresponds to $x/c = 0.008$.

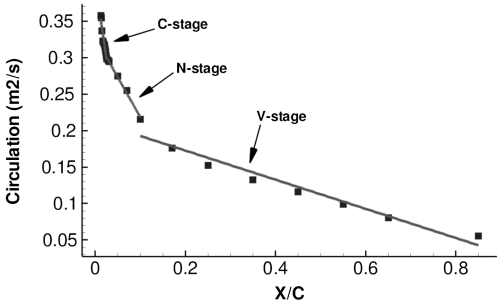

Fig. 24 Positive circulation along x/c.

clean case. Thus, downstream of the DVG the shape factor remains low for $x/c < 0.5$ (Fig. 20). However, the vortex strength rapidly decreases further downstream of the DVG, because the various interactions increase wall friction and viscous dissipation. Moreover, some local boundary-layer separation is observed during the C stage because of the orbital motion induced by the corotating interaction. Momentum is, thus, transferred from the boundary layer to the external flow and to some extent the boundary layer is perturbed. Hence, further downstream the shape factor reaches high values (Fig. 20) for $x/c > 0.5$. The boundary layer is more sensitive to the adverse pressure gradient compared to the clean case due to the DVG-induced boundary-layer perturbations. This would follow the statement made in [12] that a mixing device may increase the boundary-layer energy but also always induces a loss of momentum.

The strong initial circulation decrease reduces the vortex strength and, therefore, the stall control efficiency. Tracing this penalty the four vortices and their subsequent interactions are closely related to the DVG thickness. A reduction of the DVG thickness is then considered in the next section.

C. Deployable Vortex Generator with Reduced Thickness

The role of the DVG thickness can be analyzed by thinner DVG (tDVG) numerical simulations. Here the tDVG thickness is reduced to one-fifth (i.e., 0.2 mm) of its original size and the tDVG near-wall discretization is reduced for the local grid to match the surrounding cell sizes. Every other geometrical, numerical, or physical parameter remains unchanged. It can be noted that steady RANS computations provide satisfactory lift coefficient convergence in this case. Unfortunately, no experimental data are available in order to asses the tDVG simulations.

DVG and tDVG lift and pitching moment coefficients are presented in Fig. 25. At 12 deg both cases show very similar features. Above 15 deg tDVG and DVG show increasing discrepancies; the tDVG lift is then always higher, and no moment stall occurs for the computed AoA (even if lift stall may occur for AoA higher than 18 deg). This is promising because the tDVG delays significantly the stall compared to the DVG. The flow topology shown in Fig. 26 is simpler than for the DVG. Two positive vortices P1 and P2 are generated from the longitudinal edges of the DVG. However, P1 is much stronger and no corotating interaction is observed, and P2 rapidly merges with P1 without specific effect. A negative vortex N1 is induced through wall-vortex interaction between P1 and the airfoil wall and remains in the near-wall region. The spanwise analysis of the boundary-layer integral thicknesses downstream of both tDVG and DVG provides further understanding of the wall-vortex interactions. The spanwise shape factor at various chordwise positions shows the vortices' influence on the local boundary layer (Fig. 27). Downstream of the DVG at $x/c = 0.02$ the corotating positive vortices merge. Because of their orbital motion they are confined close to the wall, and the strong influence on the near-wall flow still

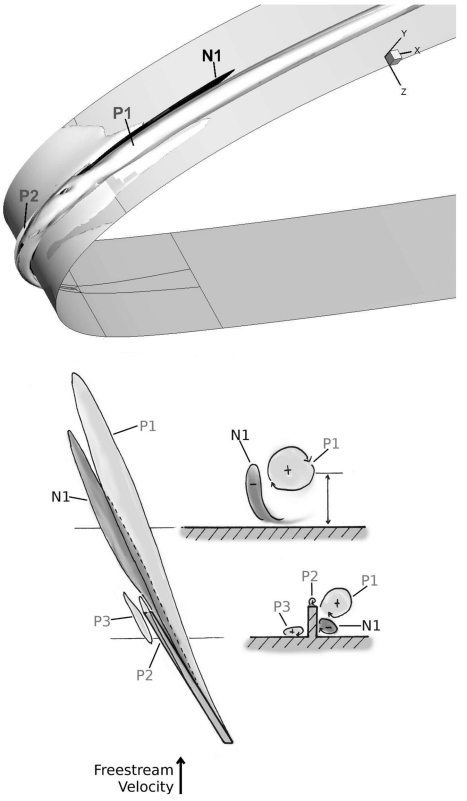

Fig. 26 tDVG flow: (top) isosurfaces of helicity and (bottom) topology sketch.

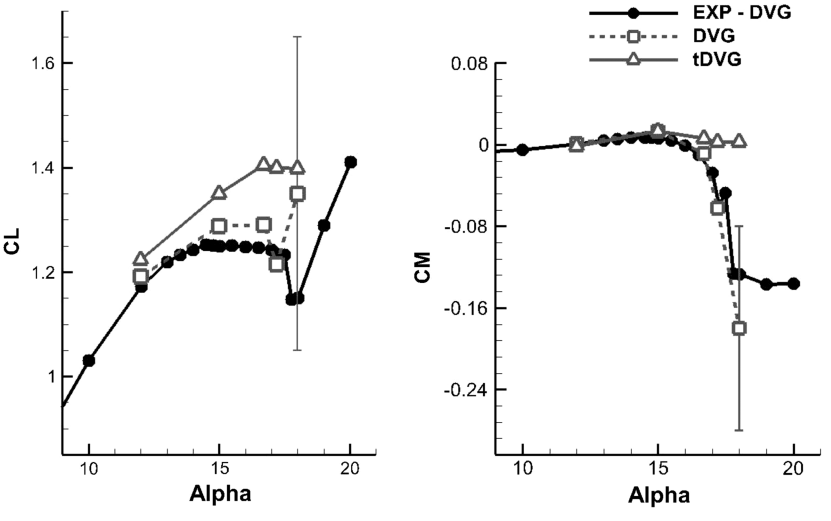

Fig. 25 DVG and tDVG polars: numerical errors bars are the min-max values.

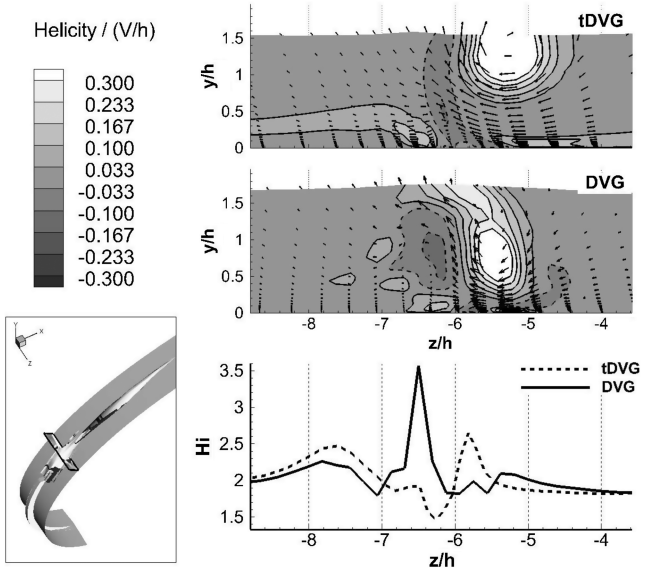

Fig. 27 Spanwise H_i and helicity comparison for DVG and tDVG at $x/c = 0.02$.

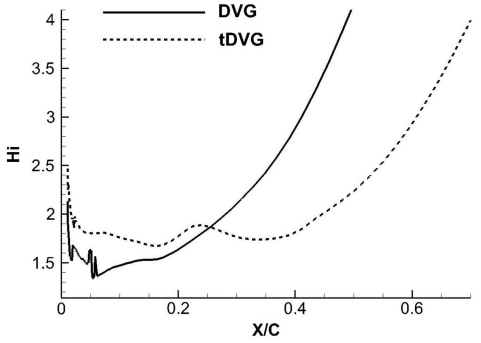

Fig. 28 Boundary-layer mean shape factor H_i along the airfoil chord $\alpha = 16.7$ deg.

initiates a separation shown by the high H_i values. In contrast, the tDVG vortex remains far from the wall and cannot induce local separation, which is shown by the lower H_i values.

The local separations observed in the early stage of the DVG corotating vortex interaction are a major drawback for stall control. On one hand, thanks to the vortices' rotating motion, momentum is injected from the outer part of the flow into the boundary layer. On the other hand, because of the wall-vortex interaction, vorticity eruption occurs as viscous response to the vortex influence. In a recent study in [33] concerning VG efficiency vortex-induced boundary-layer disturbances are investigated, and the lowest possible circulation is proved to give the best results on the adverse pressure gradient separation. In the comparison of the current cases the DVG yields higher momentum losses than the tDVG. The chordwise evolution of the spanwise-averaged shape factor H_i brings further evidence of this (Fig. 28), because the tDVG shape factor is mostly lower compared to

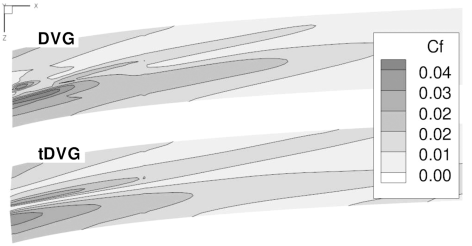

Fig. 29 Friction coefficient Cf at the upper surface of the DVG and tDVG airfoils $\alpha = 16.7$ deg.

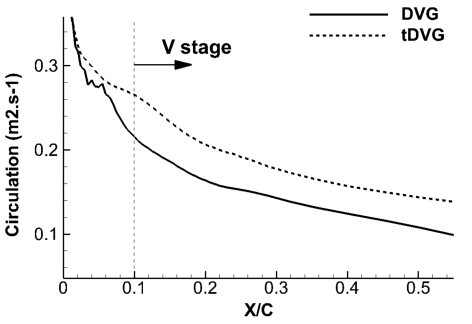

Fig. 30 Positive circulation of the DVG and tDVG at $\alpha = 16.7$ deg.

the DVG case. At $x/c = 0.4$ the shape factor of the DVG corresponds to the airfoil boundary-layer separation when tDVG separation occurs further downstream than $x/c = 0.5$.

As a consequence of the reduced wall-vortex interaction wall friction is lower for the tDVG compared to the DVG (Fig. 29). Furthermore, the tDVG circulation overall decay is lower compared to the DVG case (Fig. 30), and in the first 5% of the chord the tDVG shows a slightly lower decay rate compared to the DVG. Thus, the vortex interaction occurring downstream of the DVG is the major difference between tDVG and DVG flow. After 10% of the chord the circulation decay rates are very similar; the viscous and turbulent dissipation (the V stage) being very similar for both cases.

The longitudinal vortex efficiency for airfoil stall control is related to 1) the energy injected from the outer flow toward the inner regions of the boundary layer and 2) the boundary-layer disturbance created by the vortex presence. The tDVG achieves a better disturbance-to-mixing balance and is, therefore, more efficient for stall control.

V. Conclusions

In the present paper, the investigations and results of the OA209 airfoil static stall control using a leading-edge deployable vortex generators (DVG) are described. The methodology used for numerical simulations is presented, and a grid refinement study is provided. Boundary-layer refinement and spanwise refinements are evaluated. Although the refinement around the DVG shows no significant influence, a minimal grid density in the spanwise direction was found necessary. The computational results of the DVG are successfully compared to experimental pressure, laser Doppler velocimetry (LDV), and particle image velocimetry (PIV) data.

From the results several points are shown to be crucial in the stall control mechanism: 1) the DVG influence on the airfoil boundary layer is identified as positive in the first 45% of the chord and negative downstream, which explains the airfoil leading-edge to trailing-edge stall modification; 2) the vortex generation proves to be highly complex with the combination of several vortices because of the DVG thickness; 3) three successive stages for the main vortex physics are identified in relation to the vortex interaction modes, and these interactions are suspected to determine the stall control efficiency; and 4) numerical simulations of a DVG with reduced thickness or thinner DVG (tDVG) brings confirmation of the influence of the DVG thickness over static stall control effectiveness. tDVG is more efficient than DVG for stall alleviation.

Thanks to numerical simulations the connection between overall stall control effects and the very fine flow structures occurring around the DVG could be established. This could lead to further improvement of the DVG shape and position in future studies or experiments. A modeling of the DVG actuator may provide further computational cost reduction and could be implemented using the present results and understanding of the DVG physics. Experimental data acquisition relative to the tDVG should be considered in future wind-tunnel testings in order to assess the corresponding numerical simulations. Eventually, numerical simulations of DVG dynamic stall control will be considered for the study followup.

Acknowledgments

This work has been part of the ONERA and DLR joint project Advanced SIMulation and COntrol of Dynamic Stall (SIMCOS). We gratefully acknowledge Frederic David from the ONERA for the postprocessing of part of the experimental data. We highly appreciated the help of Markus Raffel and Karen Mulleners from the Institute of Aerodynamics and Flow Technology at DLR along with the advices of Vincent Brion from the Experimental and Fundamental Aerodynamic Department at ONERA.

References

[1] McCroskey, W. J., and Fisher, R. K. Jr., "Detailed Aerodynamic Measurements on a Model Rotor in the Blade-Stall Regime," *Journal of the American Helicopter Society*, Vol. 17, No. 1, 1972, pp. 20–30. doi:10.4050/JAHS.17.20

[2] McAlister, K. W., and Tung, C., "Suppression of Dynamic Stall with a Leading-Edge Slat on a VR-7 Airfoil," NASA TR-TP-3357, 1993.

[3] Chandrasekhara, M., Wilder, M. C., and Carr, L. W., "Unsteady Stall Control Using Dynamically Deforming Airfoils," *AIAA Journal*, Vol. 36, No. 1792, 1998, pp. 1792–1800. doi:10.2514/3.14050

[4] Mai, H., Dietz, G., Geissler, W., Richter, K., Bosbach, J., Richard, H., and DeGroot, K., "Dynamic Stall Control by Leading Edge Vortex Generators," *Journal of the American Helicopter Society*, Vol. 53, No. 26, 2008, pp. 26–36. doi:10.4050/JAHS.53.26

[5] Martin, P., Berry, J., Wong, T. C., Moulton, M., and McVeigh, M., "Passive Control of Compressible Dynamic Stall," AIAA Paper 2008-7506, 2008.

[6] Le Pape, A., Costes, M., Joubert, G., David, F., and Deluc, J.-M., "Dynamic Stall Control Using Deployable Leading-Edge Vortex Generators," *AIAA Journal*, Vol. 50, No. 10, 2012, pp. 2135–2145. doi:10.2514/1.J051452

[7] Johari, H., Henoch, C., Custodio, D., and Levshin, A., "Effects of Leading-Edge Protuberance on Airfoil Performance," *AIAA Journal*, Vol. 45, No. 11, 2007, pp. 2634–2641. doi:10.2514/1.28497

[8] Favier, J., Pinelli, A., and Piomelli, U., "Control of the Separated Flow Around an Airfoil Using a Wavy Leading Edge Inspired by Humpback Whale Flippers," *Comptes Rendus Mecaniques*, Vol. 340, Nos. 1–2, Jan.–Feb. 2012, pp. 107–114. doi:10.1016/j.crme.2011.11.004

[9] Heine, B., Mulleners, K., Joubert, G., and Raffel, M., "Dynamic Stall Control by Passive Disturbance Generator," AIAA Paper 2011-3371, 2011.

[10] Heine, B., Schanz, D., Schröder, A., Dierksheide, U., and Raffel, M., "Investigation of the Wake of Low Aspect Ratio Cylinders by Tomographic Piv," *9th International Symposium on Particle Image Velocimetry — PIV11*, Kobe, Japan, 21–23 July 2011.

[11] Taylor, H. D., "The Elimination of Diffuser Separation by Vortex Generators," United Aircraft Corp., Research Dept. Rept. R-4012-3, 1947.

[12] Schubauer, H. D., and Spangenberg, W. G., "Forced Mixing in Boundary Layers," *Journal of Fluid Mechanics*, Vol. 8, No. 1, 1960, pp. 10–32. doi:10.1017/S0022112060000372

[13] Pearcey, H. H., *Boundary Layer and Flow Control*, Pergamon Press, Oxford, England, 1961.

[14] Shabaka, I. M. M. A., Metha, R. D., and Brashaw, P., "Londitudinal Vortices Imbedded in Turbulent Boundary Layers. Part 1. Single Vortex," *Journal of Fluid Mechanics*, Vol. 155, June 1985, pp. 37–57. doi:10.1017/S0022112085001707

[15] Angele, K. P., and Muhammad-Klingmann, B., "The Effect of Streamwise Vortices on the Turbulence Structure of a Separating Boundary Layer," *European Journal of Mechanics B/Fluids*, Vol. 24, No. 5, 2005, pp. 539–554. doi:10.1016/j.euromechflu.2005.01.005

[16] Liu, J., Piomelli, U., and Spalart, P. R., "Interaction Between a Spatially Growing Turbulent Boundary Layer and Embedded Streamwise Vortices," *Journal of Fluid Mechanics*, Vol. 326, Nov. 1996, pp. 151–179. doi:10.1017/S0022112096008270

[17] Lin, J. C., Howard, F. G., and Selby, G. V., "Small Submerged Vortex Generators for Turbulent Flow Separation Control," *Journal of Spacecraft and Rockets*, Vol. 27, No. 5, 1990, pp. 503–507. doi:10.2514/3.26172

[18] Lin, J. C., "Review of Research on Low-Profile Vortex Generators to Control Boundary-Layer Separation," *Progress in Aerospace Science*, Vol. 38, Nos. 4–5, 2002, pp. 389–420. doi:10.1016/S0376-0421(02)00010-6

[19] Allan, B. G., Yao, C. S., and Lin, J. C., "Numerical Simulations of Vortex Generator Vanes and Jets on a Flat Plate," AIAA Paper 2002-3160, 2002.

[20] Gazaix, M., Jolles, A., and Lazareff, M., "The elsA Object-Oriented Computational Tool for Industrial Application," *23rd ICAS Conference*, Sept. 2002.

[21] Edward, J. R., and Liou, M. S., "Low Diffusion Flux-Splitting Methods for Flows at all Speeds," *AIAA Journal*, Vol. 36, 1998, pp. 1610–1617. doi:10.2514/3.14013

[22] Menter, F. R., "Zonal Two-Equations k-Omega Turbulence Model for Aerodynamic Flows," *AIAA Journal*, Vol. 32, No. 8, 1994, pp. 1598–1605. doi:10.2514/3.12149

[23] Arnal, D., Habiballah, M., and Coustols, E., "Laminar Instability Theory and Transition Criteria in Two- and Three-Dimensional Flow," *La Recherche Aérospatiale*, Vol. 2, 1984, pp. 125–143.

[24] Richter, K., Le Pape, A., Knopp, T., Costes, M., Gleize, V., and Gardner, A. D., "Improved Two-Dimensional Dynamic Stall Prediction with Structured and Hybrid Numerical Methods," *Journal of the American Helicopter Society*, Vol. 56, No. 4, 2011, pp. 1–12. doi:10.4050/JAHS.56.042007

[25] Thibert, J. J., and Gallot, J., "Advanced Research on Helicopter Blade Airfoils," *Vertica*, Vol. 5, 1981, pp. 279–300.

[26] Gleize, V., Costes, M., Le Pape, A., and Richez, F., "Numerical Simulation of a Pitching Airfoil Under Dynamic Stall Conditions Including Laminar/Turbulent Transitions," AIAA Paper 2008-391, Jan. 2008.

[27] Szydlowski, J., and Costes, M., "Simulation of Flow Around a NACA0015 Airfoil for Static and Dynamic Stall Configurations Using RANS and DES," *4th Decenial Specialist's Conference on Aeromechanics*, San Francisco, CA, 2004.

[28] Costes, M., Gleize, V., Szydlowski, J., Sankar, L., Guzel, G., and Rhee, M., "Grid Sensitivity Study for the Turbulent Viscous Flow Around a Naca0015 Airfoil at Stall,"*31st European Rotorcraft Forum*, Florence, Italy, Sept. 2005.

[29] Anderson, E. A., Wright, C. T., and Lawton, T. A., "Experimental Study of the Structure of the Wingtip Vortex," AIAA Paper 2000-269, Jan. 2000.

[30] Uzun, A., and Youssuf Hussaini, M., "Simulations of Vortex Formation Around a Blunt Wing Tip," *AIAA Journal*, Vol. 48, No. 6, 2010, pp. 1221–1234. doi:10.2514/1.J050147

[31] Doligalski, T. L., Smith, C. R., and Walker, J. D. A., "Vortex Interactions with Walls," *Annual Review of Fluid Mechanics*, Vol. 26, No. 1, 1994, pp. 573–616. doi:10.1146/annurev.fl.26.010194.003041

[32] Meunier, P., Le Dizes, S., and Leweke, T., "Physics of Vortex Merging," *Comptes Rendus Physiques*, Vol. 6, Nos. 4–5, 2005, pp. 431–450. doi:10.1016/j.crhy.2005.06.003

[33] Lögdberg, O., Angele, C., and Alfredsson, P. H., "On the Robustness of Separation Control by Streamwise Vortices," *European Journal of Mechanics B/Fluids*, Vol. 29, No. 1, 2009, pp. 9–17. doi:10.1016/j.euromechflu.2009.09.001

G. Blaisdell
Associate Editor